THE JOURNAL OF PHYSICAL CHEMISTRY C
A JOURNAL OF THE AMERICAN CHEMICAL SOCIETY

pubs.acs.org/JPCC

Article

Vibrational Structures of Iodine-Vacancy Bismuth Oxyiodides Using Temperature-Dependent Low-Wavenumber Raman Spectroscopy

Hsueh Han Yang,[§] Kang-Yu Hsiao,[§] Fu-Yu Liu, Chiing-Chang Chen,* and I-Chia Chen*

Cite This: *J. Phys. Chem. C* 2024, 128, 563−570

Read Online

ACCESS | Metrics & More | Article Recommendations | Supporting Information

ABSTRACT: The reaction of BiOI to form iodine-poor derivatives under high temperatures was investigated by using temperature-dependent low-wavenumber Raman spectroscopy. The Raman spectra of BiOI and of the iodine-poor derivatives $Bi_4O_5I_2$, $Bi_7O_9I_3$, and Bi_5O_7I were recorded. The phonon mode displacement vectors were calculated in the software CRYSTAL, and the PBE0/pob-TZVP method was used to analyze these Raman bands. The appearance of a Raman band at 95 cm^{-1} of a heated sample of BiOI in the atmosphere was assigned to the production of $Bi_4O_5I_2$, and up to 623 K, no other iodine-poor derivatives were generated. After 632.8 nm laser irradiation under vacuum for a few minutes before exposure to the atmosphere, $Bi_7O_9I_3$ and β-Bi_2O_3 were produced at various laser powers. Red shifts of low-wavenumber bands with temperature were obtained, and the slopes of the linear dependence χ for three phonon modes of BiOI were obtained. The obtained χ values were more negative in the atmosphere than in a vacuum. This can be explained by the reaction of BiOI to form $Bi_4O_5I_2$, during which the lattice volume may have been further expanded. The near-IR emission intensity of photoexcited BiOI was found to decrease with temperature. This turnoff process with a low activation energy is explained by thermal quenching of charge carriers.

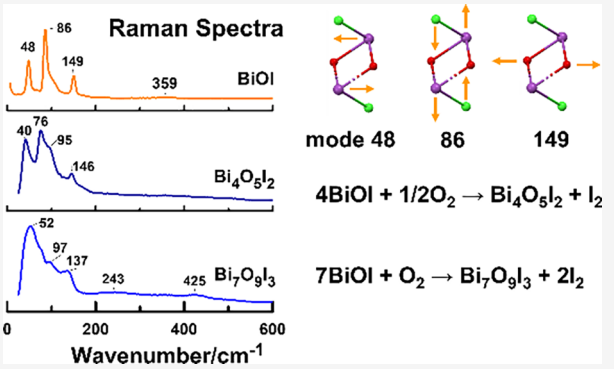

1. INTRODUCTION

Bismuth oxyhalides (BiOX, X = Cl, Br, and I), photocatalytic materials, have received considerable attention for use in many applications, such as solar water splitting, CO_2 reduction, and elimination of pollutants.[1−19] They exhibit layered structures (as shown in Figure 1); the Bi atom has covalent bonding with four O and X atoms to form a monolayer of X−Bi−O−Bi−X, and these layers are stacked by the van der Waals force between the halide ions.[3,20] For BiOI, O 2p and I 5p orbitals of the valence band and the Bi 6p orbital contribute to the conduction bands. Accordingly, this unique structure exhibits an internal electrical field perpendicular to the layers to separate the electron and hole and to avoid hole−electron recombination.[3,10] Bismuth oxyhalides activated by high temperatures or photoexcitation produce surface oxygen vacancies to provide reactive sites for inert species such as CO_2 and NO.[16]

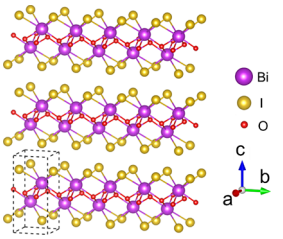

Figure 1. Layered structure of BiOI and a unit cell lattice in dotted lines.

The band gap of ∼1.8 eV and broad absorption in the visible region of BiOI make it an excellent photocatalyst under sunlight irradiation. Fan et al.[10] activated BiOI nanosheet using ultrasound to reduce the band gap to 1.74 eV and studied its photoreduction on HCHO. They found that with the activated catalyst BiOI, the HCHO to CO_2 transformation efficiency was nearly 99%. Less emission intensity for these activated materials was observed, and they exhibited electron paramagnetic resonance (EPR) activity. Hence, the researchers proposed that the oxygen vacancy in the materials was increased by irradiation and also that the formation of low electron−hole recombination resulted in an increase in catalytic efficiency.

Received: October 5, 2023
Revised: December 13, 2023
Accepted: December 14, 2023
Published: December 28, 2023

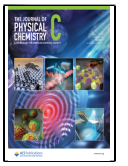

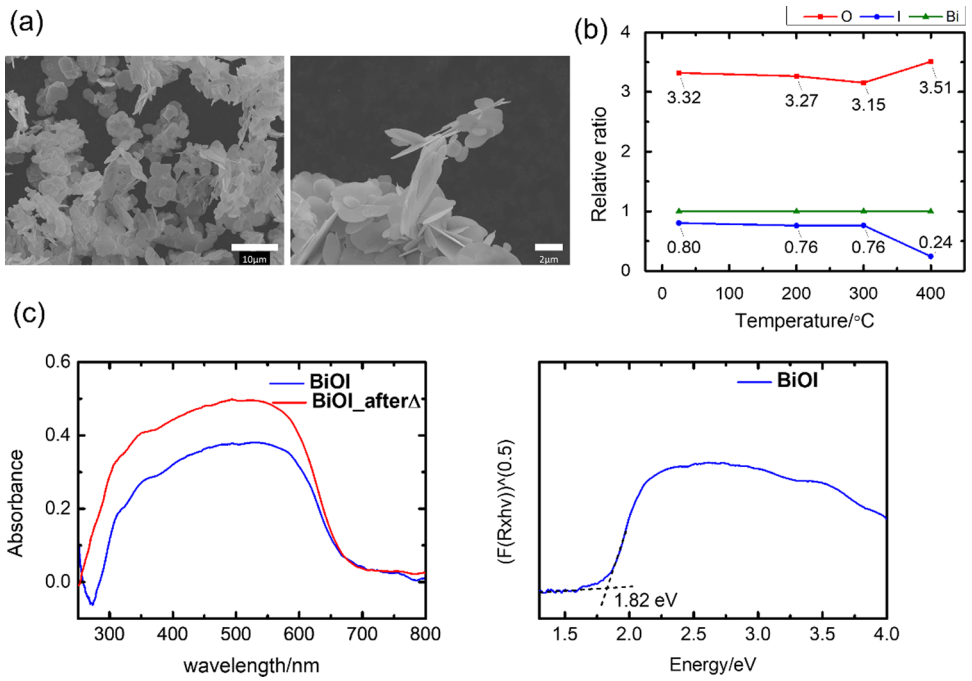

Figure 2. (a) SEM images of BiOI with scale bars of 10 μm (left) and 2 μm (right). (b) EDX of BiOI measured at 298, 473, 573, and 673 K showing that the relative amounts of the O increased and the I decreased at T = 673 K. (c) Diffusion reflectance curves (left) and Tauc plot of BiOI from diffuse reflectance spectra for BiOI before and after heating to 623 K for 30 min (right).

Recently, the photocatalytic performance of BiOI was found to be further improved by annealing to form iodine-poor derivatives $Bi_4O_5I_2$, $Bi_7O_9I_3$, and Bi_5O_7I.[18,21−24] They can be formed via the following reactions:

$$4BiOI + 1/2O_2 \rightarrow Bi_4O_5I_2 + I_2 \quad (1)$$

$$7BiOI + O_2 \rightarrow Bi_7O_9I_3 + 2I_2 \quad (2)$$

$$5Bi_4O_5I_2 + 3/2O_2 \rightarrow 4Bi_5O_7I + 3I_2 \quad (3)$$

$$5Bi_7O_9I_3 + 2O_2 \rightarrow 7Bi_5O_7I + 4I_2 \quad (4)$$

$$4Bi_5O_7I + O_2 \rightarrow 10Bi_2O_3 + 2I_2 \quad (5)$$

These iodides have increased band gaps to improve their redox ability. High photocatalytic activity has been observed in the composite materials $Bi_7O_9I_3/Bi_5O_7I$.[18] Putri et al.[24] prepared BiOI film on FTO glass and found that the band gap of the heated materials increased from 1.76 to 2.11 eV for temperatures of 373 to 830 K. They reported that at 830 K, the Raman bands 310 and 460 cm^{-1} appeared, and they assigned the bands to β-Bi_2O_3 resulting from reaction with oxygen.

Iodine vacancy at high temperatures for the formation of these iodine-poor derivatives of BiOI has been proposed. The low-wavenumber Raman spectra, also called terahertz Raman spectra, comprise lattice phonon mode information, and in many cases, these lattice modes have strong Raman scattering intensities, which could possibly provide a convenient means of identifying the bonding strengths of Bi−O and Bi−I. Moreover, specific frequencies correspond to certain vibrational modes of a specific structure, which can be used to identify these iodides, and the positions of Raman bands can be varied under the influence of the surrounding environment, such as temperature and pressure. Lu et al.[20] studied the lattice dynamics of layered BiOCl and assigned several Raman bands. They found that up to 500 K, the monolayer structure remained stable. In the present work, we studied the stability and reaction of BiOI by temperature-dependent low-wavenumber Raman spectroscopy. From the features of Raman spectra, we identified the BiOI derivatives after losing the iodide and during the annealing process. The software was employed to analyze the phonon modes and intensities to facilitate band assignments. The near-infrared (NIR) emissions of BiOI were detected under a vacuum at various temperatures to study the charge carrier dynamics.

2. EXPERIMENTAL SECTION

2.1. Materials and Characterization. BiOI nanosheets were synthesized by hydrothermal method as described elsewhere.[18] Briefly, about 2.425 g of $Bi(NO_3)_3{\cdot}5H_2O$ was dissolved in 4 M, 5 mL of HNO_3(aq), and NaOH(aq) was added to the solution until pH = 1. Then 5 M KI was added into the mixture, and after vigorous stirring, the mixture was transferred into a 100-mL Teflon-sealed autoclave and heated at 150 °C for 12 h. After cooling to room temperature, the products were collected by suction filtration, washed with distilled water several times, and dried at 60 °C for 8 h. Bi_5O_7I, $Bi_4O_5I_2$, and $Bi_7O_9I_3$ were synthesized using similar procedures but with varied molar ratios of $Bi(NO_3)_3{\cdot}5H_2O$/KI, pH values, and reaction temperatures following previous methods.[18]

The structures of BiOI, $Bi_4O_5I_2$, $Bi_7O_9I_3$, and Bi_5O_7I were identified by X-ray diffraction (XRD) patterns (Cu Kα radiation). Scanning electron microscopy energy dispersive X-ray spectroscopy (SEM-EDS) measurements were performed on a HITACHI SU-1510 F. Diffuse reflectance UV−vis curve measurements were collected with a SCINCO (S-3100) spectrometer. The XRD pattern, SEM images, and diffusion reflectance curves are shown in Figure 2. The tauc plot of BiOI is shown in the same figure; the band gap was 1.82 eV both before and after annealing (up to 627 K).

https://doi.org/10.1021/acs.jpcc.3c06627
J. Phys. Chem. C 2024, 128, 563−570

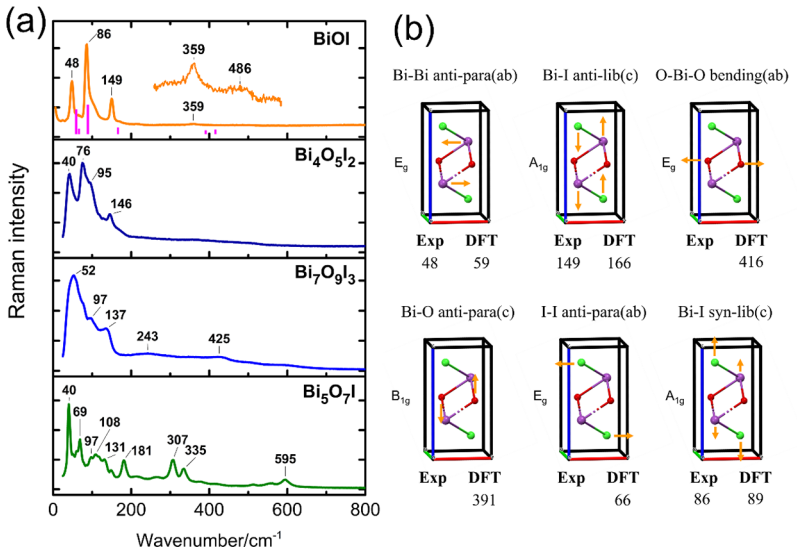

Figure 3. (a) Experimental Raman curves of BiOI (orange), $Bi_4O_5I_2$ (dark blue) $Bi_7O_9I_3$ (blue), and Bi_5O_7I (green) and the stick spectrum (pink) of calculated Raman bands of BiOI. (b) Calculated active Raman modes of BiOI (PBE0/pob-TZVP) and assigned band wavenumbers. The orange arrows denote the atomic displacement vectors of the phonon modes.

The Raman spectra were obtained from a backscattering geometry spectrometer. Samples were irradiated by an objective lens (10×) with a 632.8 nm He−Ne laser. The Raman signal passed through an edge filter, two Brag grate notch filters, an optical fiber, and a monochromator (length 0.5 m, grating 600 grooves/mm) before being detected with a liquid-nitrogen-cooled charge-coupled device (CCD, iHR550). The laser power was set at ∼9 mW in the sample region. The resolution of the spectra was typically 3−4 cm^{-1}, and each spectrum was collected for 10−60 s and averaged from 10 scans.

For temperature-controlled measurements in the range of 77−625 K, the Linkam sample stage (THMS350 V) was used. The samples were purged with nitrogen to avoid water condensation. To avoid oxygen, the sample cell was pumped by a scroll pump, and the pressure was reduced to 10^{-3} kPa. For some cases, the laser power was decreased to ∼2.5 mW to prevent overheating. The setup for NIR emission measurement was the same as the Raman system described above except that in some cases, the grating was changed to 150 grooves/mm for a wider wavelength range (650−950 nm).

2.2. Calculation Methods. Unit cell optimizations and Raman band calculations of BiOI were executed in the Crystal 17 package.[25] Several density functional theory (DFT) methods, such as PBE0, PBE0-D3, and B3LYP, were used to obtain the geometries and lattice parameters. Among them, the hybrid GGA PBE0[26,27] yielded the lattice constants closest to the experimental data, and the basis sets used were pob-TZVP for all the elements.[28,29] The optimization criteria were as follows: the maximum and RMS of gradient were set as 0.00045 and 0.00030; the maximum and RMS of displacement were 0.0018 and 0.0012 Å; the maximum trust radius was 4 Å; and the threshold of energy change was 10^{-7} Hartree. The tolerances for Coulomb and exchange sums were 10^{-6}, and the convergence on energy was 10^{-7} Hartree.

3. RESULTS AND ANALYSIS

3.1. Raman Spectra. The Raman spectra of BiOI, $Bi_4O_5I_2$, $Bi_7O_9I_3$, and Bi_5O_7I recorded at 296 K and the calculated stick spectrum of BiOI are shown in Figure 3. Varied shapes and sizes of materials with less-ordered layered structures yielded slightly varied band positions in these low-wavenumber regions. For example, the 48 cm^{-1} band of BiOI varied from 40 to 55 cm^{-1} and the 86 cm^{-1} band from 76 to 90 cm^{-1}, but the spectral features were similar. A Raman curve with the sharp spectral feature of BiOI is shown in Figure 3, revealing that the sample contained more defined and ordered layered structures.

The optimized lengths of the unit cells a and c of BiOI crystal from calculation were 3.996 and 9.221 Å, respectively. Compared with the experimental data of 3.994 and 9.149 Å,[30] the deviation of the unit cell c constant was greater, and it is likely that the calculated van der Waals force between iodides was slightly underestimated. The 59 cm^{-1} mode (cal., symmetry E_g) with large Raman intensity for Bi−Bi antiparallel displacement along the ab plane (shown in Figure 3) was assigned to the observed phonon band at 48 cm^{-1}. The 89 cm^{-1} mode (A_{1g}), also with a large Raman intensity for Bi−I antiparallel displacement along the *c* axis, was assigned to the observed band at 86 cm^{-1}. The weak 66 cm^{-1} mode for I−I antiparallel displacement was assigned to the shoulder band next to the 48 cm^{-1} band. The Bi−I libration displacement mode at 166 cm^{-1} was assigned to the observed band at 149 cm^{-1}. Two calculated O−Bi−O antiparallel stretch and bending modes were at 391 (B_{1g}) and 416 cm^{-1} (E_g), respectively, with more intensity for the latter mode. In this region, only the experimental band at 359 cm^{-1} showed prominent intensity; hence, it was assigned to an O−Bi−O mode; the exact motion was unassigned. These assignments agreed with those of Rieger et al.[31] on BiOI for the 86 and 149 cm^{-1} bands and the O−Bi−O modes of Ferrer et al.[32] on BiOBr.

Because the lattice structures of some of the iodine-poor BiOI derivatives have less-ordered crystalline structures,[33] the calculated Raman spectra of these materials could not be obtained by simply using the CRYSTAL software. In general, the spectral feature of $Bi_4O_5I_2$ was broad and similar to that of BiOI, indicating similar molecular structures. $Bi_4O_5I_2$ had bands centered at 40, 76/95, and 146 cm^{-1}. The 86 cm^{-1} band in BiOI split to 76/95 cm^{-1}, indicating that this sample had

https://doi.org/10.1021/acs.jpcc.3c06627
J. Phys. Chem. C 2024, 128, 563−570

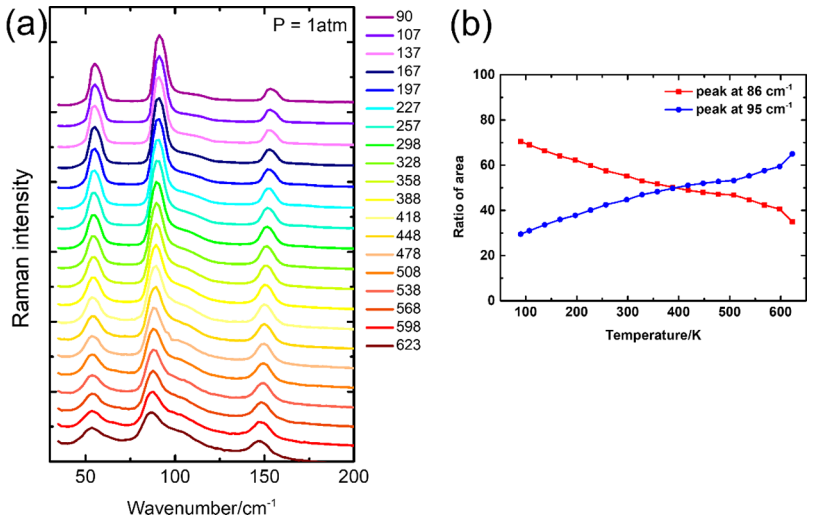

Figure 4. (a) Raman curves of BiOI in the wavenumber range of 25−200 cm^{-1} recorded in the temperature range of 90−623 K and under atmosphere. (b) The intensity ratio of the bands at 86 and 95 cm^{-1} plotted versus temperature.

varied Bi−I bonding. $Bi_7O_9I_3$ also had a broadband feature showing less-ordered layered molecular structures: roughly, the broad bands were centered at 52, 97, and 137 cm^{-1} and two weak bands at 243 and 425 cm^{-1}. B_5O_7I had relatively sharp bands and different spectral features: the 307 and 355 cm^{-1} bands lay at positions similar to the Bi−O stretch of β-Bi_2O_3. Indeed, Bi_5O_7I has an orthorhombic crystal structure, a more three-dimensional crystal structure than two-dimensional for BiOI.[34] This more defined molecular packing probably yielded sharp spectral band features.

3.2. Reactions of BiOI. The Raman spectra of BiOI recorded at varied temperatures under atmosphere and vacuum conditions are displayed in Figures 4 and S2, respectively. Each spectrum at a given temperature point was acquired for ∼5 min with a 30 K interval in the temperature range of 90−623 K. The sample was allowed to equilibrate at each temperature point for 10 min before acquisition of the next spectrum. Under the atmosphere, as the temperature increased, the intensity of the shoulder band at ∼95 cm^{-1} increased. If the sample cell was evacuated to vacuum, this shoulder band was undetected at temperatures up to 623 K. The normalized intensities of the 86 and 95 cm^{-1} bands plotted versus temperature are displayed in Figure 4 (right). From the data of SEM-EDX obtained for the annealed BiOI under atmosphere, it appears that the oxygen content increased and the iodide content clearly decreased at 673 K (Figure 2b), showing that the materials reacted with oxygen at high temperatures but lost iodides. Although the Raman curves were only recorded for temperatures up to 623 K, the same reaction may have begun at lower temperatures. Hence, we tentatively assigned the appearance of the shoulder band to the formation of $Bi_4O_5I_2$ after comparison with the measured Raman spectra of the iodine-poor derivatives. Accordingly, $Bi_4O_5I_2$ gradually formed and became the major species at high temperatures. Up to 623 K, no other iodine-poor derivatives formed.

Sample cells under vacuum were irradiated with He−Ne laser power of ∼16 mW for 1 and 6 min, respectively, at 296 K without liquid N_2 cooling to regulate the temperature, and the Raman curves are displayed in Figure 5. In these conditions, the bands became broad, and a shoulder band near 113 cm^{-1} and a new band at 309 cm^{-1} appeared. Iodide was eliminated more rapidly under vacuum; then, when the sample cell was opened to air, the samples rapidly reacted with oxygen to produce the final product β-Bi_2O_3. If the laser power was kept low at around 6 mW to avoid overheating, then after 6 min and exposure to the atmosphere, the samples were converted to $Bi_7O_9I_3$; the corresponding Raman curves are shown in Figure 5e,f. These spectra were reproducible under similar procedures.

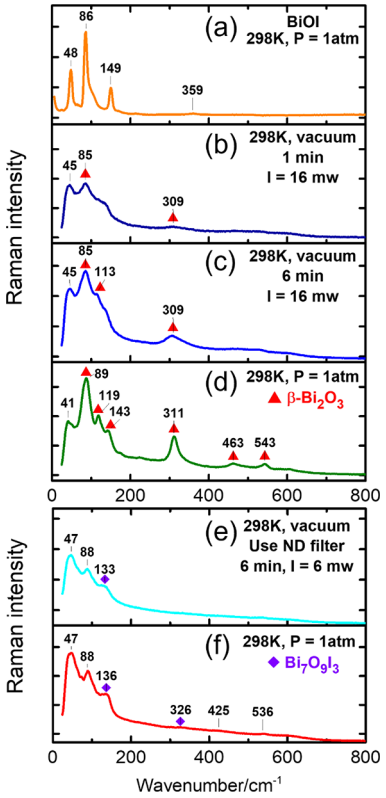

Figure 5. Raman spectra of BiOI recorded at 298 K (a) under atmosphere, (b) after evacuation and heating for 1 min with 16 mW HeNe laser, (c) for 6 min of laser radiation, and then (d) back to the atmosphere condition to form β-Bi_2O_3. Raman spectra of BiOI sample recorded at 298 K (e) in vacuum and then heated for 6 min with 6 mW HeNe laser and (f) then back to the atmosphere condition to form $Bi_7O_9I_3$.

https://doi.org/10.1021/acs.jpcc.3c06627
J. Phys. Chem. C 2024, 128, 563−570

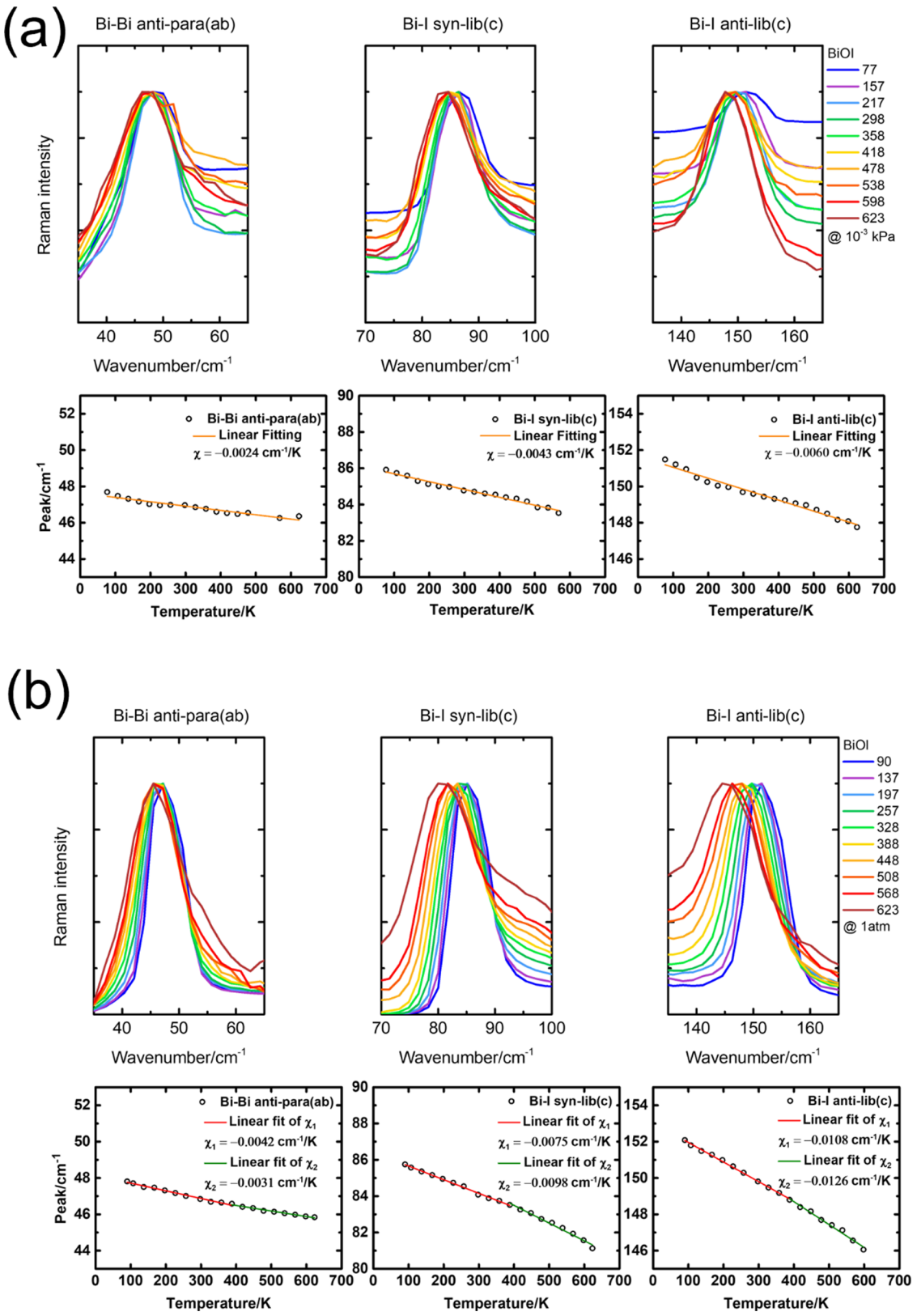

Figure 6. Bands of BiOI at 48, 86, and 149 cm^{-1} recorded at varied temperatures and peak positions plotted versus temperature in (a) vacuum and (b) atmosphere. The slopes of the best fitted lines yielded the χ values shown in the figure. In (b), the χ values were fitted for the data points below and above 400 K.

However, in either case, Bi_5O_7I could not be produced by the laser heating method.

3.3. Temperature Dependence of BiOI Raman Bands.

The shifts of the low wavenumber bands at 48, 86, and 149 cm^{-1}, measured under vacuum and atmosphere conditions,

https://doi.org/10.1021/acs.jpcc.3c06627
J. Phys. Chem. C 2024, 128, 563−570

were plotted versus temperature and are shown in Figure 6. Red shifts of band positions were contributed mainly by two factors: anharmonic phonon−phonon coupling and thermal expansion. The volume of the lattice increased with temperature, resulting in decreases in the phonon frequencies. Here, the phonon mode frequency was approximated to be linearly dependent on temperature with a slope χ, as shown in eq 6[35−37]:

$$\omega(T) = \omega_0 + \chi T \quad (6)$$

where ω_0 is the wavenumber of a band at zero Kelvin. From the measured band positions, we determined the χ values of the 48, 86, and 149 cm^{-1} modes to be −0.0024, − 0.0043, and −0.0060 cm^{-1}/K in vacuum and −0.0037, −0.0081, and −0.0115 cm^{-1}/K in atmosphere, respectively. The χ values (listed in Table 1) were more negative in the atmosphere than in vacuum. We would expect that χ should be less affected by such a small pressure difference. This can be explained by the reaction with oxygen and loss of iodides to form $Bi_4O_5I_3$ resulting in a further increase in lattice volume. BiOI was gradually converted to $Bi_4O_5I_3$ at high temperatures. Hence, we also fitted the χ value for data points below and above 400 K to yield −0.0075/−0.0098 cm^{-1}/K for the 86 cm^{-1} mode and −0.0108/−0.0126 cm^{-1}/K for the 149 cm^{-1} mode. However, the 48 cm^{-1} mode had the opposite trend, −0.0042/−0.0031 cm^{-1}/K. This mode had smaller $|\chi|$ values. Its phonon motion was mainly for Bi−Bi displacement along the ab plane and showed less sensitivity to temperature.

Table 1. Values of χ (cm^{-1}/K) of BiOI under Atmosphere (1 atm) and Vacuum, and $\Delta\chi$ is the Difference between Them

mode	χ (1 atm)	χ (vacuum)	$\Delta\chi$
48 cm^{-1} Bi−Bi antipara (ab)	−0.0037	−0.0024	−0.0035
86 cm^{-1} Bi−I syn-lib (c)	−0.0081	−0.0043	−0.0043
149 cm^{-1} Bi−I antilib (c)	−0.0115	−0.0060	−0.0070

3.4. Temperature-Dependent Emissions. The emissions of BiOI in vacuum were recorded in the wavelength range of 640−780 nm and the temperature range of 77−623 K. The emissions were less in atmosphere than in vacuum and monotonically decreased with temperature; the curves of emissions at 77, 107, 127, 157, 187, 217, 247, and 298 K are shown in Figure 7. Only the total intensity of emissions plotted versus temperature below 300 K is shown in the same figure. This NIR emission was first reported for BiOI in vacuum. With 632.8 nm light, BiOI can be excited to the conduction band directly to generate electrons and holes; their recombination can either emit light back to the ground state or relax nonradiatively. The emission band peaked at ∼655 nm at low temperatures but decreased rapidly in intensity and shifted to longer wavelengths with temperature. Bhosale et al.[38] used a transient absorption technique to study the excited states; they excited BiOI at 490 nm and probed the stimulated emission bands at wavelengths of 700, 850, and 1150 nm. They identified the detected transients as energy gap edge states, shallow trap states, and deep trap states. Based on their assignments, we detected the emissions mostly from the energy gap edge and shallow trap states.

The decrease in emission behavior with temperature can be attributed to thermal collisional quenching of charge carriers. This quenching mechanism can be described with the equation shown below[39]:

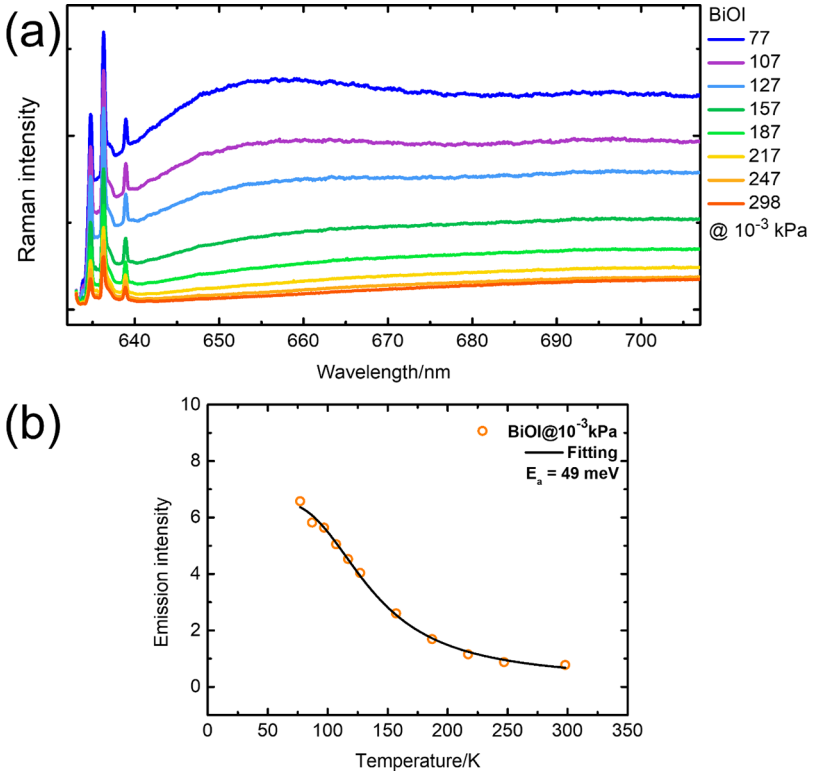

Figure 7. (a) Emission of BiOI detected in a vacuum, in the wavelength range of 633−780 nm and temperature of 77−298 K as indicated. (b) Emission intensity plotted versus temperature and a fit to eq 7 to a quenching activation energy E_a = 49 meV.

https://doi.org/10.1021/acs.jpcc.3c06627
J. Phys. Chem. C 2024, 128, 563−570

$$I(T) = \frac{I_0}{1 + Ae^{-E_a/k_BT}} \quad (7)$$

where I_0 is the emission intensity at zero Kelvin, and A and E_a are the probability factor and activation energy of decay, respectively. The fitted curve is shown in Figure 7. The E_a value was 49 meV, which is comparable to the thermal energy of charge carriers. Hence, thermal collisional quenching is the main nonradiative pathway of photoexcited BiOI.

4. DISCUSSION

Our experimental results showed that BiOI underwent gradual reaction to form $Bi_4O_5I_2$ at relatively lower temperatures. Under moderate laser irradiation, the sample was heated at a focused point to reach high temperatures to produce $Bi_7O_9I_3$. At high laser radiation, much higher temperatures were reached to produce the final product β-Bi_2O_3 directly. At temperatures greater than 623 K, the formation of iodine-poor derivatives resulted in iodine vacancies in BiOI after annealing. With the present experimental methods of low-temperature heating and laser irradiation, Bi_5O_7I could not be produced. BiOI suffered from thermal quenching in charge carriers and resulted in a reverse activation behavior; i.e., fewer charge carriers at high temperatures. In addition, at high temperatures, we observed no normal activation behavior to form a thermally activated material. Instead, at much greater temperatures, BiOI tended to react to form the iodide-poor derivatives, some of which have been found to have better catalytic efficiency.[18]

The phonon frequency can be influenced by the surrounding environment, such as the temperature and pressure. In the present work, the pressure variation was insufficient to cause any noticeable changes in sample volume simply due to the pressure factor and then to affect the phonon frequency. Carrier dynamics and heat conduction are also strongly affected by phonon vibrations, especially anharmonic phonon−phonon coupling. The χ value of graphite was measured to be -0.0011 cm^{-1}/K,[40] and that of MoS_2, ~ -0.0016 cm^{-1}/K;[41] these $|\chi|$ values are much smaller than our measured $|\chi|$ values. This also confirms the instability of the BiOI lattice with temperature.

5. CONCLUSIONS

The temperature-dependent Raman and emission spectra of BiOI were measured. The calculated Raman spectra were compared by using the PBE0/pob-TZVP method for BiOI, and all phonon bands were assigned. Notably, the DFT PBE0 method seemed to work the best, as indicated by comparison to the experimental data. The Raman spectra of the other iodine-poor derivatives of bismuth oxyiodides, $Bi_4O_5I_2$, $Bi_7O_9I_3$, and Bi_5O_7I, were measured and used to identify the reaction products of BiOI. BiOI underwent iodide loss and reaction with oxygen to form $Bi_4O_5I_2$ under atmosphere. Using laser radiation to reach high temperatures, $Bi_7O_9I_3$ and β-Bi_2O_3 were generated.

For phonon-shift with temperature, the slope χ of the linear red shift for three modes of BiOI was obtained, and the values of χ were always more negative for samples held in atmosphere. This difference is explained by reaction with oxygen molecules and the loss of iodine to form iodine-poor derivatives. The NIR emission intensity of BiOI decreased with temperature, and from the fitted activation energy of 49 meV, we determined that the decay of excitons is mainly due to thermal quenching of charge carriers. From this study, we found that BiOI cannot be activated thermally; instead, it is converted to other iodine-poor derivatives at high temperatures.

■ ASSOCIATED CONTENT

Supporting Information

The Supporting Information is available free of charge at https://pubs.acs.org/doi/10.1021/acs.jpcc.3c06627.

Experimental details of SEM-EDX, XPS, and diffuse reflectance measurements, XRD, SEM-EDX, and emission spectra, and Raman spectra in 90−623 K and under vacuum of BiOI (PDF)

■ AUTHOR INFORMATION

Corresponding Authors

Chiing-Chang Chen − *Department of Science Education and Application, National Taichung University of Education, Taichung 40306, Taiwan*; Email: ccchen@mail.ntcu.edu.tw

I-Chia Chen − *Department of Chemistry, National Tsing Hua University, Hsinchu, Taiwan 300044, Republic of China*; orcid.org/0000-0002-5821-6416; Email: icchen@mx.nthu.edu.tw

Authors

Hsueh Han Yang − *Department of Chemistry, National Tsing Hua University, Hsinchu, Taiwan 300044, Republic of China*

Kang-Yu Hsiao − *Department of Chemistry, National Tsing Hua University, Hsinchu, Taiwan 300044, Republic of China*

Fu-Yu Liu − *Department of Chemistry, National Tsing Hua University, Hsinchu, Taiwan 300044, Republic of China; Department of Science Education and Application, National Taichung University of Education, Taichung 40306, Taiwan*

Complete contact information is available at: https://pubs.acs.org/10.1021/acs.jpcc.3c06627

Author Contributions

[§]H.H.Y. and K.-Y.H. contributed equally to this work.

Notes

The authors declare no competing financial interest.

■ ACKNOWLEDGMENTS

We are grateful to the Ministry of Science and Technology of the Republic of China (MOST 110-2113-M-007-018, 111-2113-M-007-028) for financial support of this research and M. Hayashi for access to the CRYSTAL software and computation facilities.

■ REFERENCES

(1) Yu, C.; Fan, C.; Yu, J. C.; Zhou, W.; Yang, K. Preparation of Bismuth Oxyiodides and Oxides and Their Photooxidation Characteristic under Visible/UV Light Irradiation. *Mater. Res. Bull.* **2011**, *46*, 140−146.

(2) Guan, M.; Xiao, C.; Zhang, J.; Fan, S.; An, R.; Cheng, Q.; Xie, J.; Zhou, M.; Yu, B.; Xie, Y. Vacancy Associates Promoting Solar-Driven Photocatalytic Activity of Ultrathin Bismuth Oxychloride Nanosheets. *J. Am. Chem. Soc.* **2013**, *135*, 10411−10417.

(3) Li, J.; Yu, Y.; Zhang, L. Bismuth Oxyhalide Nanomaterials: Layered Structures Meet Photocatalysis. *Nanoscale* **2014**, *6*, 8473−8488.

(4) Lee, W. W.; Lu, C.-S.; Chuang, C.-W.; Chen, Y.-J.; Fu, J.-Y.; Siao, C.-W.; Chen, C.-C. Synthesis of Bismuth Oxyiodides and Their Composites: Characterization, Photocatalytic Activity, and Degradation Mechanisms. *RSC Adv.* **2015**, *5*, 23450−23463.

(5) Pan, M.; Zhang, H.; Gao, G.; Liu, L.; Chen, W. Facet-Dependent Catalytic Activity of Nanosheet-Assembled Bismuth Oxyiodide Microspheres in Degradation of Bisphenol A. *Environ. Sci. Technol.* **2015**, *49*, 6240−6248.
(6) Wu, D.; Wang, B.; Wang, W.; An, T.; Li, G.; Ng, T. W.; Yip, H. Y.; Xiong, C.; Lee, H. K.; Wong, P. K. Visible-Light-Driven BiOBr Nanosheets for Highly Facet-Dependent Photocatalytic Inactivation of Escherichia coli. *J. Mater. Chem. A* **2015**, *3*, 15148−15155.
(7) Fan, W.; Li, H.; Zhao, F.; Xiao, X.; Huang, Y.; Ji, H.; Tong, Y. Boosting the Photocatalytic Performance of (001) BiOI: Enhancing Donor Density and Separation Efficiency of Photogenerated Electrons and Holes. *Chem. Commun.* **2016**, *52*, 5316−5319.
(8) Chou, S.-Y.; Chen, C.-C.; Dai, Y.-M.; Lin, J.-H.; Lee, W. W. Novel Synthesis of Bismuth Oxyiodides/Graphitic Carbon Nitride Nanocomposites with Enhanced Visible-Light Photocatalytic Activity. *RSC Adv.* **2016**, *6*, 33478−33491.
(9) Kong, X. Y.; Lee, W. P. C.; Ong, W.-J.; Chai, S.-P.; Mohamed, A. R. Oxygen-Deficient BiOBr as a Highly Stable Photocatalyst for Efficient CO_2 Reduction into Renewable Carbon-Neutral Fuels. *ChemCatChem.* **2016**, *8*, 3074−3081.
(10) Fan, Z.; Zhao, Y.; Zhai, W.; Qiu, L.; Li, H.; Hoffmann, M. R. Facet-dependent performance of BiOBr for photocatalytic reduction of Cr(vi). *RSC Adv.* **2016**, *6*, 2028−2031.
(11) Wang, J.; Zhang, M.; Meng, J.; Li, Q.; Yang, J. Single- and Few-layer BiOI as Promising Photocatalysts for Solar Water Splitting. *RSC Adv.* **2017**, *7*, 24446−24452.
(12) Li, J.; Li, H.; Zhan, G.; Zhang, L. Solar Water Splitting and Nitrogen Fixation with Layered Bismuth Oxyhalides. *Acc. Chem. Res.* **2017**, *50*, 112−121.
(13) Wu, J.; Li, X.; Shi, W.; Ling, P.; Sun, Y.; Jiao, X.; Gao, S.; Liang, L.; Xu, J.; Yan, W.; et al. Efficient Visible-Light-Driven CO_2 Reduction Mediated by Defect-Engineered BiOBr Atomic Layers. *Angew. Chem.* **2018**, *130*, 8855−8859.
(14) Wang, H.; Yong, D.; Chen, S.; Jiang, S.; Zhang, X.; Shao, W.; Zhang, Q.; Yan, W.; Pan, B.; Xie, Y. Oxygen-Vacancy-Mediated Exciton Dissociation in BiOBr for Boosting Charge-Carrier-Involved Molecular Oxygen Activation. *J. Am. Chem. Soc.* **2018**, *140*, 1760−1766.
(15) Wang, L.; Lv, D.; Dong, F.; Wu, X.; Cheng, N.; Scott, J.; Xu, X.; Hao, W.; Du, Y. Boosting Visible-Light-Driven Photo-oxidation of BiOCl by Promoted Charge Separation via Vacancy Engineering. *ACS Sustain. Chem. Eng.* **2019**, *7*, 3010−3017.
(16) Wang, X.; Zhou, C.; Yin, L.; Zhang, R.; Liu, G. Iodine-Deficient BiOI Nanosheets with Lowered Valence Band Maximum to Enable Visible Light Photocatalytic Activity. *ACS Sustain. Chem. Eng.* **2019**, *7*, 7900−7907.
(17) Wang, X.; Li, Q.; Zhou, C.; Zhang, R. Iodine-Vacancy $BiOI_{1-x}$ Ultrathin Sheet for Improved Visible-Light Photooxidation Activities. *Appl. Sur. Sci.* **2019**, *493*, 657−664.
(18) Siao, G.-W.; Lee, W. W.; Dai, Y.-M.; Chung, W.-H.; Hung, J.-T.; Huang, P.-H.; Lin, W.-Y.; Chen, C.-C. $BiO_xCl_y/BiO_mBr_n/BiO_pI_q$/GO Quaternary Composites: Syntheses and Application of Visible-Light-Driven Photocatalytic Activities. *J. Colloid Interface Sci.* **2019**, *544*, 25−36.
(19) Zhao, H.; Liu, X.; Dong, Y.; Xia, Y.; Wang, H.; Zhu, X. Fabrication of a Z-Scheme {001}/{110} Facet Heterojunction in BiOCl to Promote Spatial Charge Separation. *ACS Appl. Mater. Interfaces* **2020**, *12*, 31532−31541.
(20) Lu, J.; Zhou, W.; Zhang, X.; Xiang, G. Electronic Structures and Lattice Dynamics of Layered BiOCl Single Crystals. *J. Phys. Chem. Lett.* **2020**, *11*, 1038−1044.
(21) Xiao, X.; Xing, C.; He, G.; Zuo, X.; Nam, J.; Wang, L. Solvothermal Synthesis of Novel Hierarchical $Bi_4O_5I_2$ Nanoflakes with Highly Visible Light Photocatalytic Performance for the Degradation of 4-tert-Butylphenol. *Appl. Catal., B* **2014**, *148−149*, 154−163.
(22) Xia, J.; Ji, M.; Di, J.; Wang, B.; Yin, S.; He, M.; Zhang, Q.; Li, H. Improved Photocatalytic Activity of Few-Layer $Bi_4O_5I_2$ Nanosheets Induced by Efficient Charge Separation and Lower Valence Position. *J. Alloys Compd.* **2017**, *695*, 922−930.
(23) Liu, C.; Wang, X.-J. Room Temperature Synthesis of $Bi_4O_5I_2$ and Bi_5O_7I Ultrathin Nanosheets with a High Visible Light Photocatalytic Performance. *Dalton Trans.* **2016**, *45*, 7720−7727.
(24) Putri, A.; Kato, S.; Kishi, N.; Soga, T. Study of Annealing Temperature Effect on the Photovoltaic Perormance of BiOI-Based Materials. *Appl. Sci.* **2019**, *9*, 3342.
(25) Dovesi, R.; Erba, A.; Orlando, R.; Zicovich-Wilson, C. M.; Civalleri, B.; Maschio, L.; Rérat, M.; Casassa, S.; Baima, J.; Salustro, S.; et al. Quantum-Mechanical Condensed Matter Simulations with CRYSTAL. *WIREs Comput. Mol. Sci.* **2018**, *8*, 1360.
(26) Perdew, J. P.; Burke, K.; Ernzerhof, M. Generalized Gradient Approximation Made Simple. *Phys. Rev. Lett.* **1996**, *77*, 3865−3868.
(27) Ernzerhof, M.; Perdew, J. P. Generalized Gradient Approximation to The Angle- and System-Averaged Exchange Hole. *J. Chem. Phys.* **1998**, *109*, 3313−3320.
(28) Vilela Oliveira, D.; Laun, J.; Peintinger, M. F.; Bredow, T. BSSE-Correction Scheme for Consistent Gaussian Basis Sets of Double- and Triple-Zeta Valence with Polarization Quality for Solid-State Calculations. *J. Comput. Chem.* **2019**, *40*, 2364−2376.
(29) Laun, J.; Bredow, T. BSSE-Corrected Consistent Gaussian Basis Sets of Triple-Zeta Valence with Polarization Quality of the Sixth Period for Solid-State Calculations. *J. Comput. Chem.* **2021**, *42*, 1064−1072.
(30) These constants of unit cell 3.994 Å and 9.149 Å space group *P4/nmm* were determined from the powder X-ray diffraction pattern.
(31) Rieger, S.; Furmann, T.; Stolarczyk, J. K.; Feldmann, J. Optically Induced Coherent Phonons in Bismuth Oxyiodide (BiOI) Nanoplatelets. *Nano Lett.* **2021**, *21*, 7887−7893.
(32) Ferrer, M. M.; Rodrigues, J. E. F. S.; Almeida, M. A. P.; Moura, F.; Longo, E.; Pizani, P. S.; Sambrano, J. R. Theoretical Methods for Calculations of Optical Phonons on BiOBr: Analysis and Correction of Propagated Errors. *J. Raman Spectrosc.* **2018**, *49*, 1356−1363.
(33) Keller, E.; Krämer, V.; Schmidt, M.; Oppermann, H. The Crystal Structure of $Bi_4O_5I_2$ and Its Relation to the Structure of $Bi_4O_5Br_2$. *Z. Kristallogr.* **2002**, *217*, 256−264.
(34) Hassan, Q. U.; Channa, A. I.; Zhai, Q. G.; Zhu, G.; Gao, Y.; Ali, N.; Bilal, M. Recent Advancement in Bi_5O_7I-based Nanocomposites for High Performance Photocatalysts. *Chemosphere* **2022**, *288*, No. 132668.
(35) Zhu, S.; Zheng, W. Temperature-Dependent Phonon Shifts in van der Waals Crystals. *J. Phys. Chem. Lett.* **2021**, *12*, 5261−5270.
(36) Klemens, P. G. Decay of High-Frequency Longitudinal Phonons. *J. Appl. Phys.* **1967**, *38*, 4573−4576.
(37) Balkanshi, M.; Wallis, R. F.; Haro, E. Anharmonic Effects in Light Scattering due to Optical Phonons in Silicon. *Phys. Rev. B* **1983**, *28*, 1928−1934.
(38) Bhosale, A. H.; Narra, S.; Bhosale, S. S.; Liao, P. S.; Ohta, N.; Diau, E. W. G. Femtosecond Relaxation Dynamics of Two-Dimensional BiOI nanoplatelets as Efficient Photocatalysts. *J. Chin. Chem. Soc.* **2022**, *69*, 51−59.
(39) Shibata, H. Negative Thermal Quenching Curves in Photoluminescence of Solids. *Jpn. J. Appl. Phys.* **1998**, *37*, 550−553.
(40) Tan, P.; Deng, Y.; Zhao, Q.; Cheng, W. The Intrinsic Temperature Effect of the Raman Spectra of Graphite. *Appl. Phys. Lett.* **1999**, *74*, 1818−1820.
(41) Lanzillo, N. A.; Glen Birdwell, A.; Amani, M.; Crowne, F. J.; Shah, P. B.; Najmaej, S.; Liu, Z.; Ajayan, P. M.; Lou, J.; Dubey, M.; et al. Temperature-Dependent Phonon Shifts in Monolayer MoS_2. *Appl. Phys. Lett.* **2013**, *103*, No. 093102.

https://doi.org/10.1021/acs.jpcc.3c06627
J. Phys. Chem. C 2024, 128, 563−570